Research Square

Preprints are preliminary reports that have not undergone peer review.
They should not be considered conclusive, used to inform clinical practice,
or referenced by the media as validated information.

Legumain-Responsive Remodeling of Self-Assembled Peptide Nanostructures for Colorectal Cancer Therapy

Zhen Ren

dylan214@126.com

Central Hospital of Dalian University of Technology

Jingyuan Zhao

Central Hospital of Dalian University of Technology

Xinru Tang

Central Hospital of Dalian University of Technology

Ruixin Yang

Central Hospital of Dalian University of Technology

Li Shuai

Central Hospital of Dalian University of Technology

Hong Yuan

Central Hospital of Dalian University of Technology

Research Article

Keywords:

Posted Date: November 25th, 2026

DOI: https://doi.org/10.21203/rs.3.rs-11600039/v1

License: This work is licensed under a Creative Commons Attribution 4.0 International License.
Read Full License

Additional Declarations: No competing interests reported.

Legumain-Responsive Remodeling of Self-Assembled Peptide Nanostructures for Colorectal Cancer Therapy

Zhen Ren[1,2], Jingyuan Zhao[1,4], Xinru Tang[1,2], Ruixin Yang[1,2], Shuai Li[1,3,*], Hong Yuan[1,4,*]

1 Central Hospital of Dalian University of Technology, Dalian 116003, Liaoning, China
2 Faculty of Medicine, Dalian University of Technology, Dalian 116024, Liaoning, China
3 The First Affiliated Hospital of Dalian Medical University, Dalian, Liaoning, China
4 Dalian Medical-Engineering Interdisciplinary Rapid Diagnosis of Major Diseases Laboratory, Dalian, Liaoning, China

Zhen Ren and Jingyuan Zhao contributed equally to this work.
*Correspondence: Hong Yuan (yuanhonglab@163.com); Shuai Li (shuaili2015@outlook.com)

Abstract

Stimuli-responsive peptide nanostructures can couple tumor-associated delivery with localized activation, but the relationship between enzymatic processing, physicochemical remodeling, and therapeutic performance remains difficult to define. We designed SKM, a modular peptide that combines an RGD-containing targeting segment, an AAN legumain-responsive site, a KVFF self-assembly motif, a mitochondria-disrupting KLAKLAKKLAKLA segment, and an IHIHICI bioactive segment. Legumain exposure converted elongated SKM assemblies into shorter structures, reduced the mean hydrodynamic diameter from 660.6 ± 50.79 to 42.75 ± 19.09 nm, and shifted the zeta potential from -13.13 ± 2.26 to -1.1 ± 4.8 mV. SKM was internalized efficiently by HCT116 colorectal cancer cells, perturbed mitochondrial homeostasis, reduced DNA synthesis and clonogenic growth, and increased tumor-cell death. The treatment also suppressed GPX4, altered iron- and lipid-metabolism-associated markers, increased C11-BODIPY oxidation, and enhanced calreticulin expression and surface exposure. After intravenous administration to HCT116 xenograft-bearing mice, fluorescently labeled SKM accumulated preferentially in tumors, reached maximal tumor fluorescence at 8 h, and inhibited tumor growth without overt systemic toxicity under the tested conditions. These findings link legumain-responsive nanostructure remodeling to mitochondrial perturbation, ferroptosis-associated lipid stress, and antitumor activity, supporting further development of SKM as an enzyme-responsive peptide biomaterial for colorectal cancer therapy.

Keywords: peptide nanostructure; enzyme-responsive material; legumain; colorectal cancer; ferroptosis-associated stress; biointerface

Introduction

Colorectal cancer (CRC) is the third most commonly diagnosed malignancy and the second leading cause of cancer-related death in the United States [1]. Despite advances in screening and multimodal treatment, approximately 30-50% of patients experience recurrence, metastasis, or death within five years after therapy [2-4]. Surgery, chemotherapy, and radiotherapy remain central to CRC management; however, limited tumor selectivity, systemic toxicity, and the emergence of treatment resistance continue to restrict durable benefit, particularly in advanced disease [5-7]. There is therefore a pressing need for therapeutics that combine tumor-specific delivery with potent, mechanistically complementary antitumor activity.

Peptide therapeutics have emerged as an attractive class of anticancer agents because of their small molecular size, favorable biocompatibility, modularity, and potential for high target specificity. Their clinical translation, however, is frequently constrained by proteolytic instability, rapid clearance, and inefficient intracellular delivery. In parallel, immunogenic cell death (ICD) has gained attention as a strategy for converting local tumor destruction into durable antitumor immunity. During ICD, dying tumor cells expose or release damage-associated molecular patterns, including calreticulin (CRT), heat shock proteins 70 and 90, ATP, and high-mobility group box 1. These signals facilitate tumor-antigen uptake and processing by antigen-presenting cells, promote cross-presentation, and may support tumor-specific T-cell responses, thereby helping convert immunologically "cold" tumors into "hot" tumors [8-11].

Three complementary design principles may improve the therapeutic performance of anticancer peptides. First, mitochondrial targeting can rapidly disrupt tumor-cell bioenergetics and redox homeostasis, promoting cell death while potentially limiting

the development of classical drug resistance [12, 13]. Second, ferroptosis, an iron-dependent form of regulated cell death driven by lipid peroxidation, offers a means of eliminating cells that are resistant to apoptosis and may amplify oxidative stress-associated immunogenic signaling. Third, peptide self-assembly and stimulus-responsive structural remodeling can protect functional sequences, improve intracellular retention, and enable site-selective exposure of bioactive modules. Integrating these properties within a single molecule could therefore enhance delivery, ferroptosis, and ICD-associated signaling.

On this basis, we designed SKM as an enzyme-responsive peptide nanomaterial that integrates an RGD-containing targeting element, an AAN legumain-responsive site, a KVFF self-assembly motif, a mitochondria-disrupting segment, and a bioactive IHIHICI segment. We hypothesized that legumain-mediated processing would remodel the physicochemical state of the peptide and thereby alter its biological interactions at tumor-cell interfaces. We therefore linked structural and colloidal characterization to cellular uptake, mitochondrial perturbation, ferroptosis-associated lipid damage, calreticulin exposure, tumor accumulation, therapeutic efficacy, and preliminary biosafety in an HCT116 xenograft model (Fig. 1).

Figure 1

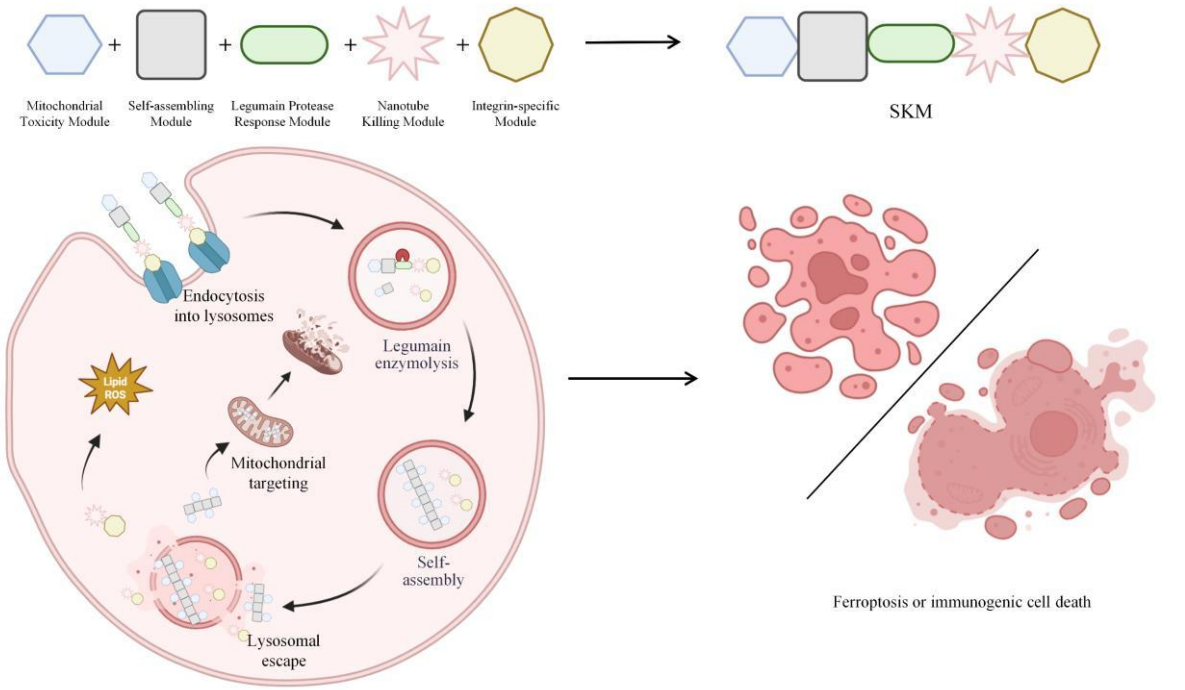

Fig. 1 Design and proposed mechanism of action of SKM. SKM comprises a mitochondrial-toxicity segment, a self-assembling segment, a legumain-responsive sequence, a bioactive nanotube-killing segment, and an integrin-targeting segment. The schematic depicts the proposed sequence of integrin-associated uptake, lysosomal delivery, legumain-triggered structural remodeling and self-assembly, lysosomal escape, mitochondrial perturbation, and lipid reactive oxygen species accumulation, leading to ferroptosis- and immunogenic cell death-associated tumor-cell injury. The mechanistic sequence is a design model and includes steps that remain to be experimentally validated

Materials and Methods

Peptide Synthesis and Preparation

The legumain-responsive precursor SKM (KLAKLAKKLAKLAKVFFAANIHIHICIRGD) was designed as a modular peptide comprising five functional elements (Fig. 1). The construct was organized, from the N terminus to the C terminus, as a KLAKLAKKLAKLA segment intended to perturb mitochondria, a KVFF self-assembly

motif, an AAN legumain-responsive cleavage site, an IHIHICI nanozyme bioactive segment, and a terminal RGD-containing targeting motif. The control peptide IHR (IHIHICIRGD) was synthesized in parallel for comparative experiments. SKM and IHR were prepared by Fmoc-based solid-phase peptide synthesis, with amino acids coupled sequentially from the C terminus to the N terminus. After chain assembly, the side-chain protecting groups were removed and the peptides were cleaved from the resin. The crude products were purified by reverse-phase high-performance liquid chromatography (RP-HPLC) and lyophilized. Peptide identity and molecular mass were verified by mass spectrometry, and chromatographic purity was evaluated by analytical RP-HPLC. Cy3-labeled SKM and IHR were prepared for cellular-uptake experiments, whereas Cy5-labeled SKM and IHR were prepared for in vivo fluorescence-imaging experiments.

Legumain-Responsive Cleavage and Morphological Characterization

To evaluate enzyme responsiveness, SKM was incubated with recombinant legumain, while an equal amount of SKM maintained in the corresponding reaction buffer without enzyme served as the untreated control. After incubation, samples were prepared for transmission electron microscopy, and their morphology was examined using a transmission electron microscope (Thermo Fisher Scientific, Waltham, MA, USA). Representative images were acquired using identical imaging settings whenever possible.

Hydrodynamic Size and Zeta Potential

The hydrodynamic diameter and zeta potential of SKM before and after legumain treatment were measured using a Zetasizer Nano-ZS90 nanoparticle analyzer (Malvern Panalytical, Malvern, UK). For hydrodynamic-size measurements, samples

were dispersed in phosphate-buffered saline (PBS); for zeta-potential measurements, samples were dispersed in pure water. Both measurements were performed at room temperature.

Preliminary Hemocompatibility Assessment

The preliminary hemocompatibility of SKM was evaluated using a hemolysis assay. Samples were incubated with SKM under the experimental conditions used in this study. PBS was used as the negative control, and double-distilled water (ddH2O) was used as the positive control. Hemolysis was evaluated relative to both controls.

Cell Lines and Culture

Human HCT116 colorectal cancer cells (CL-0096), HEK293 cells (CL-0001), MDA-MB-231 breast cancer cells (CL-0150), A549 non-small-cell lung cancer cells (CL-0016), NCI-H1299 non-small-cell lung cancer cells (CL-0165), and 769-P renal carcinoma cells (CL-0009) were purchased from Wuhan Pricella Biotechnology Co., Ltd. (Wuhan, China). HCT116 cells were cultured in DMEM supplemented with 10% fetal bovine serum and 1% penicillin-streptomycin at 37 °C in a humidified atmosphere containing 5% CO2. The other cell lines were maintained in their corresponding recommended media under the same incubation conditions. Cells in the logarithmic growth phase were used for all experiments.

Cellular Uptake

HCT116 cells were seeded in glass-bottom confocal dishes and allowed to attach for 24 h. Cells were then incubated with Cy3-labeled SKM or Cy3-labeled IHR. After treatment, the cells were washed with phosphate-buffered saline (PBS), counterstained for nuclei when required, and examined by confocal laser-scanning microscopy. Intracellular Cy3 fluorescence was acquired using the same laser power

and detector settings across treatment groups and quantified from representative fields.

Cytotoxicity and IC50 Determination

Cells in the logarithmic growth phase were seeded in 96-well plates at 10,000 cells per well in 100 μL of complete medium and allowed to attach for 24 h. Cells were exposed to a concentration series of SKM or IHR and incubated for 48 h. Cell viability was measured using the Cell Counting Kit-8 (GK10001, GLPBIO, China) according to the manufacturer's instructions. Absorbance was measured at 450 nm, and IC50 values were calculated by nonlinear regression. HCT116 cells were selected for subsequent experiments on the basis of the preliminary screening results, and HEK293 cells were used for an initial assessment of non-malignant-cell toxicity.

Propidium Iodide and Calcein-AM/PI Viability Staining

HCT116 cells were seeded in imaging-compatible culture plates, allowed to attach, and treated with the designated concentrations of SKM, IHR, or vehicle control. Loss of plasma-membrane integrity was assessed by propidium iodide staining. Live and dead cells were further visualized using the Calcein-AM/PI Cell Viability/Cytotoxicity Assay Kit (C2015S, Beyotime, China) according to the manufacturer's instructions. Fluorescence images were acquired using identical settings, and the proportions of live and dead cells were quantified from randomly selected fields.

EdU Proliferation Assay

DNA synthesis was evaluated using an EdU incorporation assay. HCT116 cells were treated with SKM, IHR, or vehicle control and then incubated with EdU. Cells were fixed, permeabilized, subjected to the EdU detection reaction, and counterstained for

nuclei according to the kit protocol. Images were acquired by fluorescence microscopy, and the percentage of EdU-positive cells was calculated relative to the total number of nuclei.

Colony-Formation Assay

HCT116 cells in the logarithmic growth phase were seeded at 1,000 cells per well in 12-well plates. After 2 days, cells were treated with the designated concentrations of SKM, IHR, or vehicle control. Colonies were allowed to develop for 14 days, washed with PBS, fixed with anhydrous ethanol, and stained with crystal violet. Colonies were counted using the same inclusion criterion for all groups. Each experimental group was analyzed in triplicate.

Mitochondrial Staining

Mitochondrial changes after peptide treatment were evaluated using MitoTracker Green. HCT116 cells were seeded in confocal dishes, treated with SKM, IHR, or vehicle control, washed with PBS, and incubated with the probe according to the manufacturer's instructions. After washing, fluorescence images were obtained using a laser confocal microscope (LSM 980, ZEISS, Germany), and mitochondrial fluorescence intensity was quantified under identical acquisition settings.

RNA Isolation and Quantitative Real-Time PCR

Total RNA was isolated from treated HCT116 cells using TRIzol reagent. Equal amounts of total RNA (1 μg) were reverse-transcribed into complementary DNA using the PrimeScript RT Reagent Kit (Takara, Kyoto, Japan). Quantitative real-time PCR was performed on a QuantStudio 6 Flex System using SYBR Green reagent (Takara, Kyoto, Japan) to quantify the mRNA expression of GPX4, PTGS2, TfR1, FHC, NCOA4, ACSL4, and CRT. Target-gene expression was normalized to

GAPDH and calculated using the 2^(-ΔΔCt) method. The primers were synthesized by Sangon Biotech (China). Each sample was analyzed using technical replicates, and the experiment was repeated independently. Primer sequences are summarized in Table 1.

Table 1 Primer sequences used for quantitative real-time PCR

Gene	Forward primer (5'-3')	Reverse primer (5'-3')
GAPDH	GGAGCGAGATCCCTCCAAAAT	GGCTGTTGTCATACTTCTCATGG
GPX4	GAGGCAAGACCGAAGTAAACTAC	CCGAACTGGTTACACGGGAA
PTGS2	CTGGCGCTCAGCCATACAG	CGCACTTATACTGGTCAAATCCC
TfR1	ACCATTGTCATATACCCGGTGAT	CAATAGCCCAAGTAGCCAATCAT
FHC	CCCCCATTTGTGTGACTTCAT	GCCCGAGGCTTAGCTTTCATT
NCOA4	GAGGTGTAGTGATGCACGGAA	GACGGCTTATGCAACTGTGAA
ACSL4	CATCCCTGGAGCAGATACTCT	TCACTTAGGATTTCCCTGGTCC
CRT	CCTGCCGTCTACTTCAAGGAG	GAACTTGCCGGAACTGAGAAC

Protein Extraction and Western Blotting

Following treatment, total cellular proteins were extracted from HCT116 cells using a protein extraction kit (P0028, Beyotime, China) according to the manufacturer's instructions, and protein concentrations were determined. Equal amounts of protein were separated on 10% SDS-polyacrylamide gels and transferred to polyvinylidene fluoride membranes (IPVH00010, Millipore, Germany). The membranes were blocked with 5% skimmed milk in Tris-buffered saline containing Tween-20 (TBST) and incubated at 4 °C overnight with primary antibodies against GPX4 (Cat No. 67763-1-Ig, proteintech, China), COX-2/PTGS2 (Cat No. 12375-1-AP, proteintech, China), TfR1 (Cat No. 10084-2-AP, proteintech, China), FHC (Cat No. 11682-1-AP, proteintech, China), NCOA4 (Cat No. 83394-4-RR, proteintech, China), ACSL4 (Cat No. 22401-1-AP, proteintech, China), CRT (Cat No. 27298-1-AP, proteintech, China), and GAPDH (Cat No. CPA1460, Cohesion, China). After washing, the

membranes were incubated with horseradish peroxidase-conjugated goat anti-rabbit IgG (Cat No. CSA2115, Cohesion, China) or horseradish peroxidase-conjugated anti-mouse IgG (Cat No. CSA2107, Cohesion, China). Protein bands were visualized using an enhanced chemiluminescence kit (P0018FM, Beyotime, China), quantified by densitometry, and normalized to GAPDH.

Immunofluorescence Staining

For intracellular immunofluorescence, treated HCT116 cells were fixed, permeabilized, blocked, and incubated with primary antibodies against NCOA4 (Cat No. 83394-4-RR, proteintech, China) or COX-2 (Cat No. 12375-1-AP, proteintech, China), followed by species-appropriate fluorescent secondary antibodies and nuclear counterstaining. To detect cell-surface CRT, cells were stained under non-permeabilizing conditions with an anti-CRT antibody (Cat No. 27298-1-AP, proteintech, China) before imaging. Images were acquired by confocal microscopy using identical acquisition settings for all groups, and fluorescence intensity was quantified from representative fields.

Lipid Peroxidation Assay

Lipid peroxidation was assessed using the C11-BODIPY 581/591 fluorescent probe. After treatment with SKM, IHR, or vehicle control, HCT116 cells were incubated with the probe, washed with PBS, and analyzed by fluorescence imaging or flow cytometry. Oxidation of the probe was evaluated from the shift in fluorescence from the reduced red-emitting form to the oxidized green-emitting form, and the oxidized-to-reduced fluorescence ratio was calculated.

Animals and Ethics Statement

Male BALB/c nude mice, 6 weeks of age, were purchased from Liaoning Changsheng Biotechnology Co., Ltd. (Liaoning, China) and maintained under specific-pathogen-free (SPF) conditions with free access to food and water. All animal procedures were reviewed and approved by the Ethics Committee of the Central Hospital of Dalian University of Technology (approval no. YN2026-072-01) and were performed in accordance with institutional guidelines.

HCT116 Xenograft Establishment and In Vivo Tumor Targeting

To establish the xenograft model, 5×10^6 HCT116 cells suspended in 100 μL of PBS and Matrigel were inoculated subcutaneously into nude mice. After tumors were established, mice were assigned to the in vivo targeting groups, with six animals per group. Cy5-labeled SKM or IHR was administered by tail-vein injection. During whole-body fluorescence imaging, mice were anesthetized with inhaled isoflurane, and images were acquired at 0, 4, 8, 16, and 24 h after injection. For ex vivo biodistribution analysis, mice were anesthetized by intraperitoneal injection of sodium pentobarbital (100 mg/kg; prepared in PBS at 10 mg/mL) and subsequently euthanized by decapitation while under anesthesia at 8 h after injection. The tumor, heart, liver, spleen, lung, and kidney were then collected and imaged using the same acquisition settings. Fluorescence intensity was quantified for each tissue.

In Vivo Antitumor Treatment

HCT116 tumor-bearing mice were randomly assigned to treatment groups after tumors reached the prespecified size, with six animals per group. SKM and the corresponding control treatments were administered by tail-vein injection for 18 days according to the dosing schedule used in this study. Tumor dimensions and body

weight were recorded regularly. Tumor volume was calculated as V = (length × width^2)/2. At the end of treatment, mice were anesthetized and euthanized using the same sodium pentobarbital and decapitation procedure described above; Tumors were then excised, photographed, weighed, and processed for histological analysis. Major organs and blood samples were collected for safety evaluation.

Histology, Immunohistochemistry, and TUNEL Staining

Tumors and major organs were fixed in 4% paraformaldehyde, embedded in paraffin, sectioned at 4 μm, and stained with hematoxylin and eosin. Tumor-cell proliferation was evaluated by immunohistochemical staining with an anti-Ki67 antibody (Cat No. HA721115, HUABIO, China). Apoptotic or DNA-fragmented cells in tumor sections were detected using a TUNEL assay according to the kit manufacturer's instructions. Images were acquired using a light or fluorescence microscope, as appropriate, and quantified using predefined analysis criteria.

Serum Biochemistry

At the end of treatment, blood was collected from the orbital venous plexus. Blood samples were allowed to stand at 4 °C overnight and then centrifuged, after which the serum was collected. Hepatic and renal function were evaluated by measuring serum ALT, AST, blood urea nitrogen, uric acid, and creatinine using the designated biochemical analyzer or commercial assay kits according to the manufacturers' protocols.

Statistical Analysis

Statistical analyses were performed using GraphPad Prism 7.0 (GraphPad Software, San Diego, CA, USA). Data are presented as the mean ± standard error of the mean unless otherwise stated. Comparisons between two independent groups were

performed using a two-tailed unpaired Student's t-test. Comparisons involving more than two groups were analyzed by one-way analysis of variance followed by an appropriate multiple-comparison test, while repeated tumor-growth measurements were analyzed using a two-way repeated-measures analysis of variance when applicable. Statistical significance was defined as *P < 0.05, **P < 0.01, ***P < 0.001, and ****P < 0.0001.

Results

Legumain-Responsive Remodeling and Preliminary Evaluation of SKM Nanostructures

RP-HPLC and mass spectrometry confirmed the successful synthesis and identity of SKM and IHR (Supplementary Fig. S1). The molecular masses were 3332.16 Da for SKM and 1176.41 Da for IHR, consistent with the designed peptide products. The morphological response of SKM to legumain was then examined by transmission electron microscopy (TEM). Untreated SKM formed prominent elongated fibrillar assemblies (Fig. 2A), whereas legumain treatment produced markedly shorter structures (Fig. 2B), consistent with efficient enzymatic cleavage. Dynamic light scattering further showed that the mean hydrodynamic diameter decreased from 660.6 ± 50.79 nm before cleavage to 42.75 ± 19.09 nm after legumain exposure (Fig. 2C,D), in agreement with the TEM observations. In parallel, the zeta potential shifted from -13.13 ± 2.26 mV to -1.1 ± 4.8 mV after enzymatic treatment (Fig. 2E,F). This shift toward electrical neutrality indicates that legumain treatment substantially altered the interfacial properties of the peptide assemblies.

In a preliminary hemocompatibility assay, samples exposed to SKM remained visually comparable to the PBS negative control and distinct from the ddH2O positive

control (Supplementary Fig. S2A), supporting preliminary hemocompatibility at the tested concentrations. HCT116 colorectal cancer cells showed the greatest response to SKM and were selected for subsequent mechanistic studies (Fig. 2G). Screening results for MDA-MB-231, A549, H1299, and 769P cells are presented in Supplementary Fig. S2C. Over the same concentration range, SKM showed limited toxicity toward HEK293 cells (Fig. 2H). By contrast, IHR produced little cytotoxicity in the tested tumor and non-malignant cells (Supplementary Fig. S2D), supporting the functional importance of the SKM design.

Figure 2

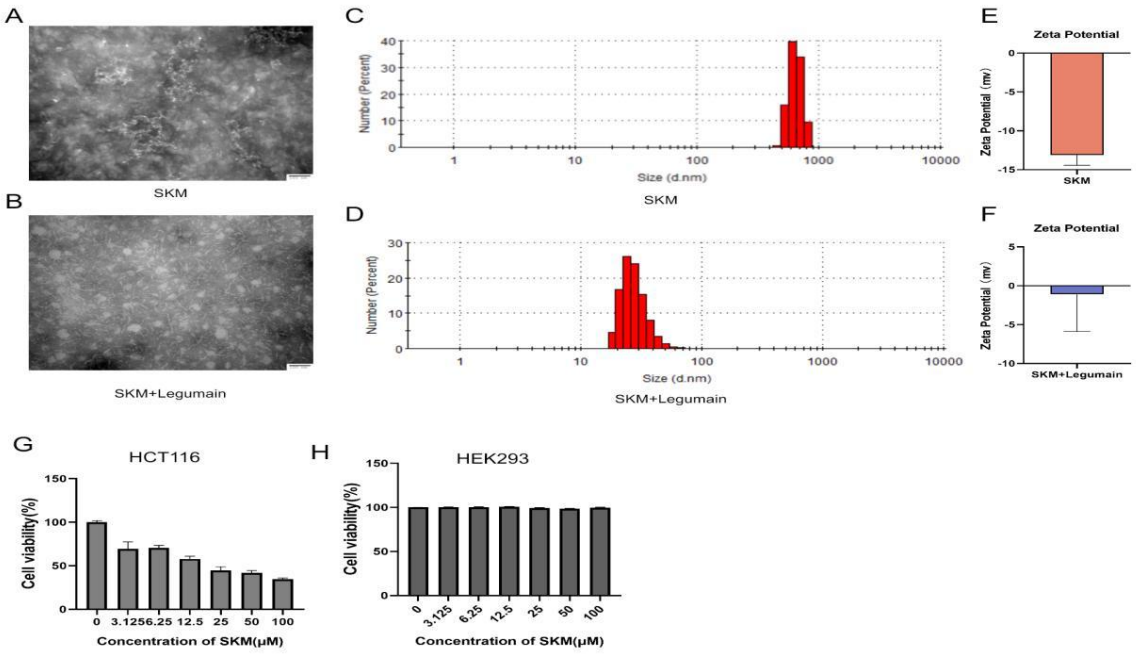

Fig. 2 Legumain-responsive physicochemical remodeling and cytotoxicity assessment of SKM. (A,B) Transmission electron microscopy images of SKM before and after legumain treatment, respectively. (C,D) Hydrodynamic-size distributions measured by dynamic light scattering before and after legumain exposure. (E,F) Zeta potentials of untreated and legumain-treated SKM measured in pure water at room temperature. (G) Concentration-dependent viability of HCT116 cells after SKM treatment. (H) Viability of HEK293 cells after SKM treatment. Data are presented as mean ± SEM where applicable; statistical annotations are defined in the Materials and Methods.n=3

Cellular Uptake, Mitochondrial Perturbation, and Antiproliferative Activity

Cellular uptake was examined using Cy3-labeled peptides. Confocal microscopy revealed strong intracellular Cy3 fluorescence after SKM treatment, whereas only weak signals were observed in the negative-control and IHR groups (Supplementary Fig. S2B), demonstrating efficient cellular internalization. MitoTracker Green staining subsequently showed a marked reduction in mitochondrial fluorescence in SKM-treated cells relative to both control groups (Fig. 3A), consistent with substantial mitochondrial perturbation.

SKM markedly increased the proportion of propidium iodide-positive cells (Fig. 3B), indicating loss of plasma-membrane integrity. EdU incorporation was substantially reduced after SKM treatment (Fig. 3C), demonstrating suppression of DNA synthesis. Consistently, Calcein-AM/propidium iodide staining showed fewer viable cells and more dead cells in the SKM group than in the control groups (Fig. 3D), while colony-formation assays confirmed a sustained decrease in clonogenic capacity (Fig. 3E). To assess an immunogenic cell death-associated response, calreticulin (CRT) was examined after peptide treatment. SKM increased CRT mRNA abundance (Fig. 3F), elevated CRT protein abundance as confirmed by immunoblotting and densitometric quantification (Fig. 3G,H), and enhanced cell-surface CRT fluorescence (Fig. 3I). Together, these findings indicate that SKM is efficiently internalized, perturbs mitochondria, promotes tumor-cell death, suppresses proliferation, and induces a CRT-associated immunogenic phenotype in HCT116 cells.

Figure 3

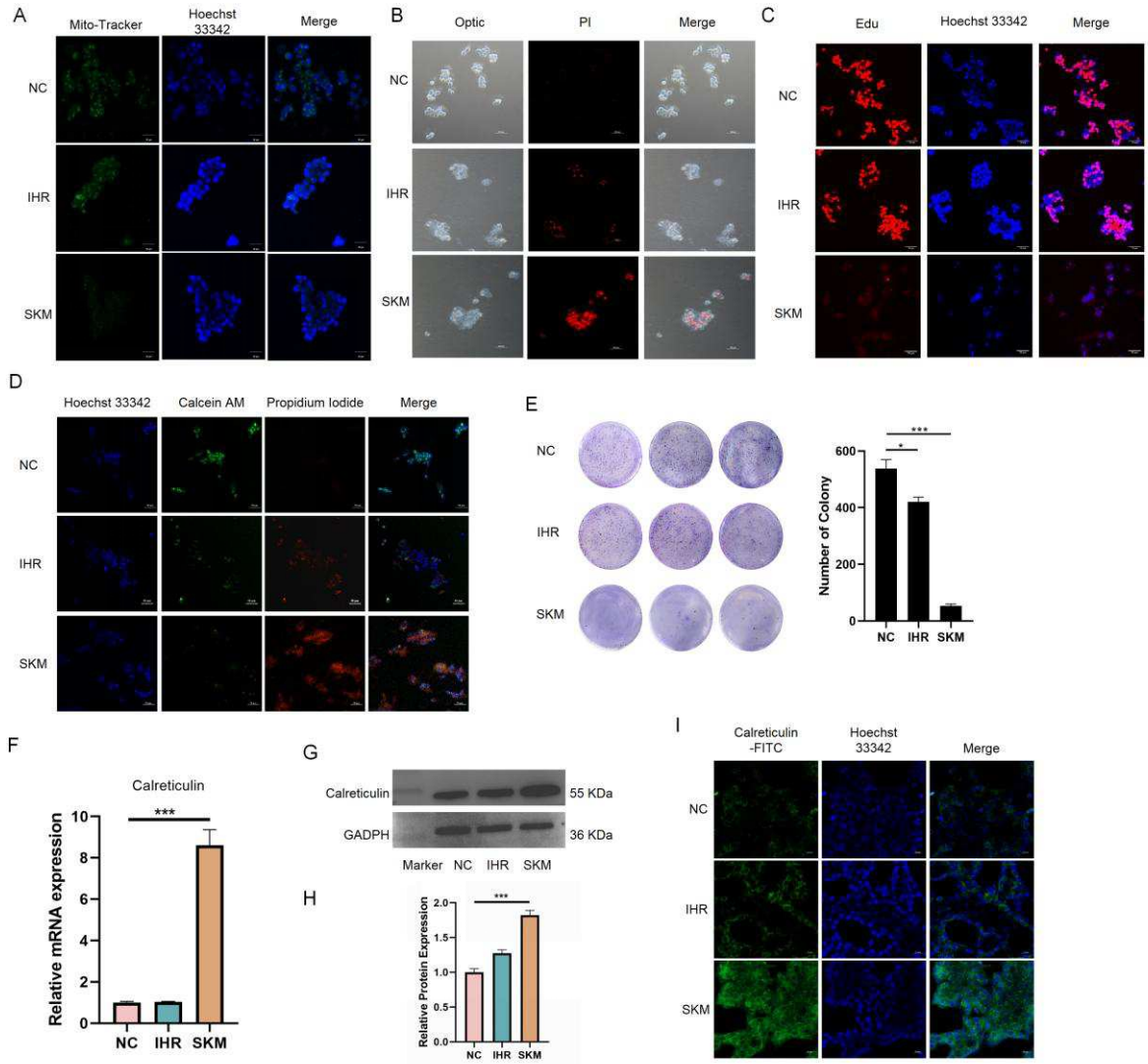

Fig. 3 SKM disrupts mitochondria, reduces viability, suppresses proliferation, and induces calreticulin in HCT116 cells. (A) MitoTracker Green staining after the indicated treatments. (B) Propidium iodide staining showing loss of plasma-membrane integrity. (C) EdU incorporation assay showing DNA synthesis. (D) Calcein-AM/propidium iodide live/dead staining. (E) Representative colony-formation images and colony-number quantification. (F) Relative CRT mRNA expression. (G) Representative immunoblot of CRT, with GAPDH as the loading control. (H) Densitometric quantification of CRT protein expression normalized to GAPDH. (I) Cell-surface CRT immunofluorescence; nuclei were counterstained with Hoechst 33342. NC, negative control; IHR, control peptide. Data are presented as mean ± SEM where applicable; statistical annotations are defined in the Materials and Methods.n=3

Ferroptosis-Associated Signaling and Lipid Peroxidation

To determine whether ferroptosis contributes to SKM-induced cytotoxicity, the expression of key ferroptosis-related genes and proteins was measured in HCT116 cells. Compared with the negative-control and IHR groups, SKM treatment reduced glutathione peroxidase 4 (GPX4) at both the mRNA and protein levels, while increasing cyclooxygenase-2/prostaglandin-endoperoxide synthase 2 (COX-2/PTGS2) (Fig. 4A-F). Transferrin receptor 1 (TfR1), ferritin heavy chain (FHC), nuclear receptor coactivator 4 (NCOA4), and acyl-CoA synthetase long-chain family member 4 (ACSL4) also changed in a pattern consistent with altered iron handling, ferritinophagy, and ferroptosis-associated lipid metabolism. Immunofluorescence staining confirmed enhanced NCOA4 and COX-2 signals after SKM treatment (Fig. 4G,H).

Lipid peroxidation was examined using the C11-BODIPY 581/591 probe. SKM treatment produced a pronounced shift from the reduced red-emitting form toward the oxidized green-emitting form (Fig. 4I), indicating extensive accumulation of lipid peroxidation products. These molecular and imaging data collectively support activation of a ferroptosis-associated response by SKM.

Fig. 4 SKM alters ferroptosis-associated signaling and lipid oxidation in HCT116 cells. (A) Relative mRNA expression of TfR1 and GPX4. (B,C) Representative immunoblots and densitometric analysis of GPX4 and FHC, with GAPDH as the loading control. (D) Relative mRNA expression of NCOA4, ACSL4, and COX-2/PTGS2. (E,F) Representative immunoblots and densitometric analysis of ACSL4 and COX-2, with GAPDH as the loading control. (G,H) Immunofluorescence images of NCOA4 and COX-2, respectively; nuclei were counterstained with Hoechst 33342. (I) C11-BODIPY 581/591 imaging of the reduced red-emitting and oxidized green-emitting probe states. NC, negative control; IHR, control peptide. Statistical annotations are shown in the corresponding panels. Data are presented as mean ± SEM where applicable; statistical annotations are defined in the Materials and Methods.n=3

Figure 4

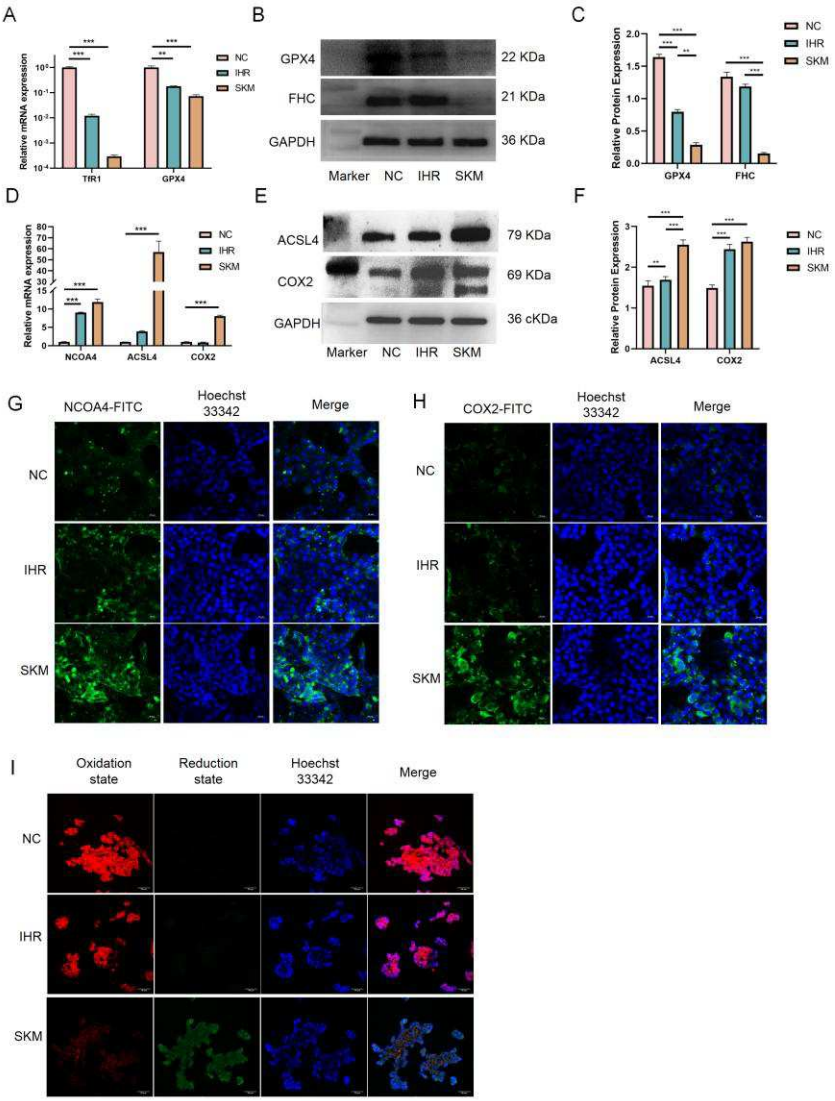

Tumor Accumulation, Antitumor Activity, and Preliminary Biosafety

Tumor accumulation was assessed by tail-vein administration of Cy5-labeled SKM or IHR to nude mice bearing HCT116 xenografts, followed by longitudinal fluorescence imaging. A detectable SKM signal appeared at the tumor site 4 h after injection, reached its maximum at 8 h, declined markedly by 16 h, and was largely cleared by

24 h (Fig. 5A,B). Ex vivo imaging at 8 h showed stronger fluorescence in tumor tissue than in the heart, liver, spleen, lung, or kidney (Fig. 5C), supporting preferential tumor accumulation under the tested conditions.

Therapeutic efficacy was then evaluated in the same xenograft model. After 18 days of treatment, tumors in the SKM group had smaller volumes and lower weights than those in the control group (Fig. 5D-G). Histological analysis showed lower tumor-cell density and reduced Ki67 staining after SKM treatment (Fig. 5H), consistent with impaired proliferation. TUNEL staining was also increased in SKM-treated tumors (Fig. 5I), indicating enhanced tumor-cell death in vivo.

Preliminary safety was evaluated throughout the treatment period. Body weight showed a modest decline across all groups during treatment, with no appreciable differences among the NC, IHR, and SKM groups (Supplementary Fig. S3A). Histological examination of the heart, liver, spleen, lung, and kidney revealed no overt treatment-related abnormalities (Supplementary Fig. S3B). In addition, serum markers of hepatic function (ALT and AST) and renal function (blood urea nitrogen, uric acid, and creatinine) showed no obvious treatment-associated shifts and were broadly comparable among groups (Supplementary Fig. S3C). These findings indicate that SKM inhibited HCT116 xenograft growth without detectable systemic toxicity under the tested dosing regimen.

Figure 5

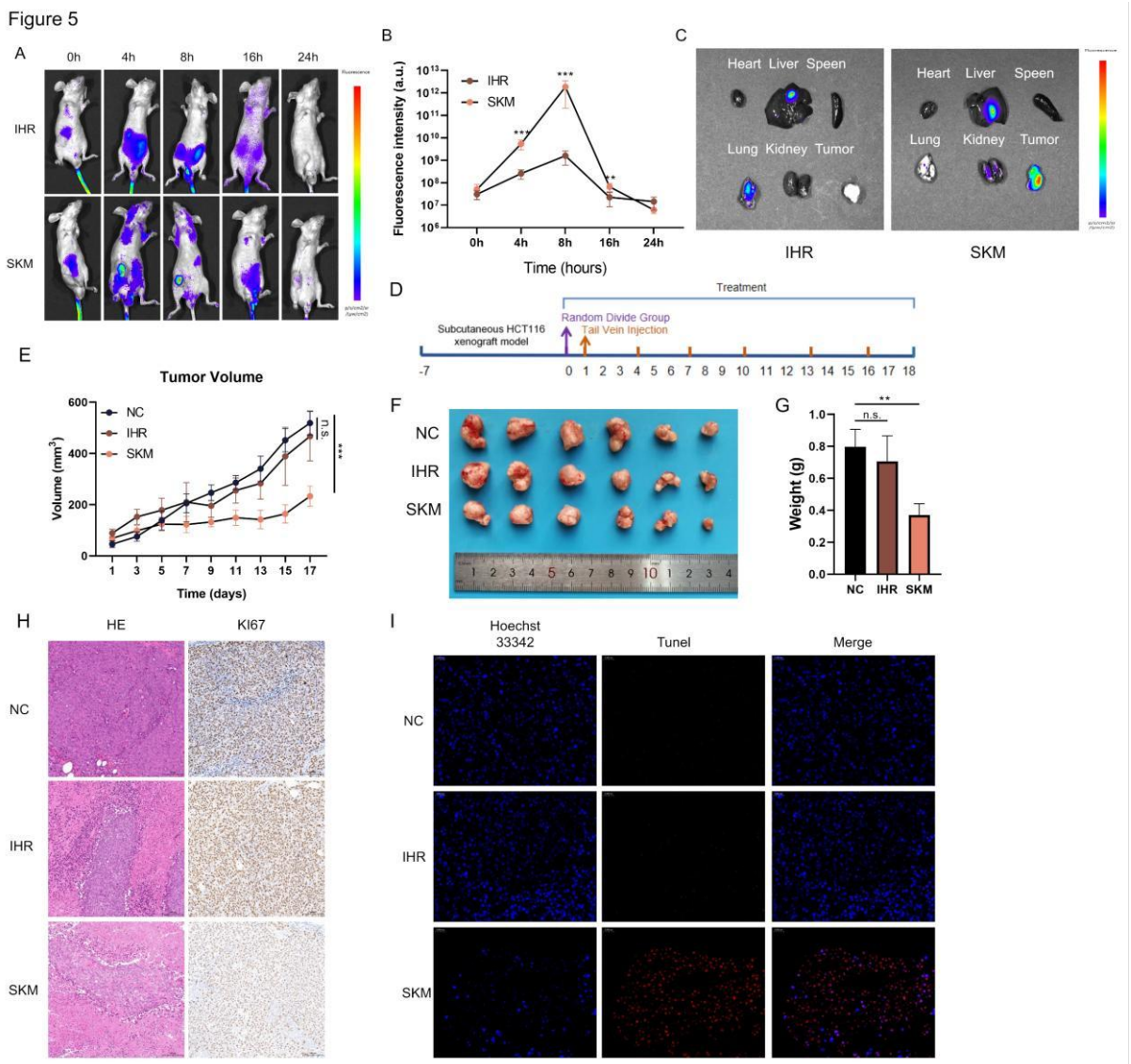

453

454 Fig. 5 Tumor accumulation, antitumor efficacy, and histological effects of SKM in
455 HCT116 xenograft-bearing mice. (A) Serial whole-body fluorescence images
456 obtained at 0, 4, 8, 16, and 24 h after tail-vein administration of Cy5-labeled IHR or
457 SKM. (B) Quantification of tumor-associated fluorescence intensity over time. (C) Ex
458 vivo fluorescence images of the heart, liver, spleen, lung, kidney, and tumor
459 collected 8 h after injection. (D) Experimental schedule for establishment and
460 treatment of the subcutaneous HCT116 xenograft model. (E) Tumor-growth curves
461 during treatment. (F) Images of excised tumors. (G) Final tumor weights. (H)
462 Hematoxylin and eosin and Ki67 staining of tumor sections. (I) Hoechst 33342,
463 TUNEL, and merged fluorescence images of tumor sections. NC, negative control;
464 IHR, control peptide. Data are presented as mean ± SEM where applicable;
465 statistical annotations are defined in the Materials and Methods.n=6

466

467

Discussion

This study establishes SKM as a modular peptide platform that couples tumor-associated uptake with enzyme-responsive structural remodeling and complementary forms of cellular stress. Legumain treatment reduced the hydrodynamic size of SKM and shifted its zeta potential toward electrical neutrality. In HCT116 cells, SKM showed greater uptake than the targeting-deficient IHR control, impaired mitochondrial homeostasis, reduced DNA synthesis and clonogenic growth, altered ferroptosis-related markers, increased lipid oxidation, and promoted calreticulin (CRT) expression. These cellular effects were accompanied by preferential tumor accumulation and suppression of xenograft growth without overt treatment-associated toxicity under the tested regimen.

The sequence architecture provides a plausible framework for these observations. The KLAKLAKKLAKLA, KVFF, AAN, IHIHICI, and C-terminal RGD-containing segments were designed to support mitochondrial perturbation, self-assembly, legumain responsiveness, bioactivity, and tumor-associated uptake, respectively. The large reduction in particle size after legumain exposure, supported by both TEM and DLS, indicates substantial physicochemical remodeling. Such remodeling could alter tissue penetration, membrane interactions, and intracellular retention [14, 15]. However, the present experiments do not directly establish integrin-specific binding, lysosomal cleavage or escape, β-sheet assembly, membrane insertion, or the identity of the active cleavage products. A non-cleavable analogue, legumain inhibition or knockdown, and direct structural analysis will be required to demonstrate enzyme dependence and define the post-cleavage assembly state. Legumain is overexpressed in human colorectal tumors and has been associated with adverse clinicopathological features, providing a disease-specific rationale for the AAN trigger

493 [16, 17]. In related work, an AAN-masked cell-penetrating carrier was reactivated by
494 legumain in tumors [18], while enzyme-instructed peptide self-assembly converted
495 enzyme activity into selective intracellular nanofiber formation and cancer-cell killing
496 [19]. The cleavage-associated shift from approximately 660 nm to 43 nm may also
497 favor interstitial transport, consistent with size-dependent tumor access reported for
498 sub-100-nm carriers [20].
499 The uptake and viability data further support, but do not prove, the proposed
500 targeting function. Cy3-SKM generated stronger intracellular fluorescence than IHR,
501 whereas IHR produced little cytotoxicity in the tested cells. These findings are
502 consistent with a contribution from the targeting segment and with prior work on
503 tumor-homing and tissue-penetrating peptides [15, 21]. Receptor-blocking,
504 competitive-binding, and integrin-knockdown experiments are nevertheless needed
505 to identify the responsible receptor and internalization pathway. Selectivity should
506 also be tested in non-malignant intestinal, hepatic, endothelial, and hematopoietic
507 cells rather than inferred from HEK293 cells alone. The RGD motif derives from the
508 canonical fibronectin cell-adhesion sequence [22], but receptor specificity remains to
509 be established in the SKM system.
510 Mitochondrial perturbation and ferroptosis-associated lipid damage appear to be
511 complementary components of SKM activity. Reduced MitoTracker Green
512 fluorescence, membrane injury, and impaired clonogenic survival indicate marked
513 cellular stress, although MitoTracker Green does not directly measure mitochondrial
514 membrane potential. Concurrent GPX4 suppression, COX-2 induction, altered TfR1,
515 FHC, NCOA4, and ACSL4 expression, and oxidation of C11-BODIPY are consistent
516 with disruption of iron handling and lipid-peroxide control [23-26]. Because marker
517 changes alone cannot establish ferroptosis, the mechanism should be tested using

ferrostatin-1 or liproxstatin-1 rescue, iron chelation, and measurements of labile iron, glutathione, and mitochondrial ultrastructure. The reported interaction between tumor ferroptosis and T-cell activity also provides a rationale for evaluating ferroptosis-immune crosstalk [27]. Mechanistically, ferroptotic execution is linked to oxidation of arachidonoyl- and adrenoyl-phosphatidylethanolamines [28] and is opposed by the FSP1-coenzyme Q pathway operating in parallel with GPX4 [29], neither of which was directly measured here.

CRT induction links direct tumor-cell injury to a possible immunogenic cell death (ICD)-associated response. Surface-exposed CRT can function as an eat-me signal for antigen-presenting cells and is an established component of ICD [30, 31]. Nevertheless, CRT exposure alone does not demonstrate a complete immunogenic antitumor response. Confirmation should include extracellular ATP and HMGB1 release, HSP70/HSP90 exposure, dendritic-cell maturation, cross-presentation, and tumor-specific T-cell activation [31, 32]. This limitation is especially important because BALB/c nude mice cannot adequately evaluate T-cell-dependent immunity. Immunocompetent syngeneic or humanized CRC models, together with tumor-rechallenge experiments, will be necessary to determine whether SKM generates durable immune protection. Foundational ICD studies further indicate that antitumor immunogenicity can involve caspase-dependent death programs, HMGB1-TLR4 signaling, ATP-P2X7-NLRP3 activation, and regulated preapoptotic CRT trafficking [33-36].

In vivo fluorescence peaked at 8 h and declined thereafter, while ex vivo imaging supported preferential tumor accumulation. SKM also reduced tumor volume, tumor weight, cellularity, and Ki67 staining and increased TUNEL positivity. However, fluorescence imaging cannot distinguish intact peptide from labeled metabolites, and

the efficacy study used one cell line, a subcutaneous model, and a relatively short treatment period. Future studies should incorporate pharmacokinetics, metabolite profiling, repeated-dose biodistribution, orthotopic or metastatic CRC models, patient-derived systems, and direct comparison with standard therapies. Safety evaluation should be expanded to hematology, hemolysis, complement activation, coagulation, cytokine release, immunogenicity, and chronic dosing. Together, these studies will determine whether SKM is best developed as a monotherapy or as a partner for chemotherapy, radiotherapy, or immunotherapy.

Conclusion

SKM integrates tumor-targeted delivery, legumain-responsive structural remodeling, mitochondrial perturbation, and ferroptosis-associated lipid damage within a single peptide platform. The peptide was efficiently internalized by HCT116 cells, suppressed proliferation, elicited an ICD-associated CRT response, accumulated preferentially in xenograft tumors, and inhibited tumor growth without overt toxicity under the tested conditions. These findings provide a strong rationale for further development of SKM while underscoring the need for definitive pathway-rescue studies, comprehensive immune validation, broader CRC models, and expanded pharmacokinetic and safety evaluation.

Supplementary Information

The Supplementary Information contains peptide characterization by reverse-phase high-performance liquid chromatography and mass spectrometry, preliminary hemocompatibility, cellular uptake and cytotoxicity controls, and preliminary in vivo safety data.

Acknowledgements

OpenAI Codex was used for English-language editing and manuscript-formatting assistance. The authors reviewed and edited the output and take full responsibility for the content of the manuscript.

Author Contributions

Z.R. and J.Z. contributed equally to this work. All authors contributed to the conception or design of the study; acquisition, analysis, or interpretation of data; drafting or critical revision of the manuscript; and approval of the final version. All authors agree to be accountable for the work.

Funding

This work was supported by the National Natural Science Foundation of China (grant 82502797), the Liaoning Provincial Key R&D Project (grant 2024JH2/102500045), and the Liaoning Provincial Science and Technology Program Joint Project (grant 2024JH2/102600013).

Data Availability

The data supporting the findings of this study are available from the corresponding authors on reasonable request.

Materials Availability

The peptide sequences and characterization data generated in this study are provided in the manuscript and Supplementary Information. Requests for additional materials should be directed to the corresponding authors.

Code Availability

Not applicable. No custom software or code was generated for this study.

Ethics Approval

All animal procedures were reviewed and approved by the Ethics Committee of the Central Hospital of Dalian University of Technology (approval no. YN2026-072-01) and were performed in accordance with institutional guidelines.

Animal Welfare

All animal procedures were conducted in accordance with the approved protocol and institutional guidelines for the care and use of laboratory animals. Mice were maintained under specific-pathogen-free conditions with free access to food and water.

Clinical Trial Registration

Clinical Trial Number: not applicable. This study did not involve human participants or a clinical trial.

Consent to Participate

Not applicable.

Consent to Publish

Not applicable.

Competing Interests

The authors declare that they have no competing financial or non-financial interests.

Author Information

Correspondence: Hong Yuan (yuanhonglab@163.com); Shuai Li (shuaili2015@outlook.com). Additional author emails: Zhen Ren (dylan214@126.com); Jingyuan Zhao (zhaojingyuanlab@outlook.com); Xinru Tang (tangxr@mail.dlut.edu.cn); Ruixin Yang (sherlockholmes@mail.dlut.edu.cn).

Abbreviations

ACSL4, acyl-CoA synthetase long-chain family member 4; ALT, alanine aminotransferase; AST, aspartate aminotransferase; CCK-8, Cell Counting Kit-8; COX-2, cyclooxygenase-2; CRC, colorectal cancer; CRT, calreticulin; DAMP, damage-associated molecular pattern; DLS, dynamic light scattering; DMEM, Dulbecco's modified Eagle medium; EdU, 5-ethynyl-2'-deoxyuridine; FHC, ferritin heavy chain; GAPDH, glyceraldehyde-3-phosphate dehydrogenase; GPX4, glutathione peroxidase 4; HPLC, high-performance liquid chromatography; HMGB1, high-mobility group box 1; HSP, heat shock protein; IC50, half-maximal inhibitory concentration; ICD, immunogenic cell death; IHR, control peptide; NC, negative control; NCOA4, nuclear receptor coactivator 4; PBS, phosphate-buffered saline; PI, propidium iodide; PTGS2, prostaglandin-endoperoxide synthase 2; RGD, arginine-glycine-aspartic acid; RP-HPLC, reverse-phase high-performance liquid chromatography; SPF, specific-pathogen-free; SKM, legumain-responsive multifunctional peptide; TBST, Tris-buffered saline containing Tween-20; TEM, transmission electron microscopy; TfR1, transferrin receptor 1; TUNEL, terminal deoxynucleotidyl transferase dUTP nick-end labeling.

References

1. Siegel RL, Kratzer TB, Wagle NS, Sung H, Jemal A. Cancer statistics, 2026. CA Cancer J Clin. 2026;76(1):e70043.
2. Zheng X, Wang Q, Zhou Y, Zhang D, Geng Y, Hu W, et al. N-acetyltransferase 10 promotes colon cancer progression by inhibiting ferroptosis through N4-acetylation and stabilization of ferroptosis suppressor protein 1 (FSP1) mRNA. Cancer Commun (Lond). 2022;42(12):1347–1366.
3. Bien J, Lin A. A Review of the Diagnosis and Treatment of Metastatic Colorectal Cancer. JAMA. 2021;325(23):2404–2405.
4. Chen W, Zheng R, Baade PD, Zhang S, Zeng H, Bray F, et al. Cancer statistics in China, 2015. CA Cancer J Clin. 2016;66(2):115–132.
5. Goc J, Lv M, Bessman NJ, Flamar AL, Sahota S, Suzuki H, et al. Dysregulation of ILC3s unleashes progression and immunotherapy resistance in colon cancer. Cell. 2021;184(19):5015–5030.e5016.
6. Kerr DJ, Chamberlain S, Kerr RS. Celecoxib for Stage III Colon Cancer. JAMA. 2021;325(13):1257–1258.
7. Siegel RL, Wagle NS, Star J, Kratzer TB, Smith RA, Jemal A. Colorectal cancer statistics, 2026. CA Cancer J Clin. 2026;76(2):e70067.

8. Green DR, Ferguson T, Zitvogel L, Kroemer G. Immunogenic and tolerogenic cell death. Nat Rev Immunol. 2009;9(5):353–363.

9. Krysko DV, Garg AD, Kaczmarek A, Krysko O, Agostinis P, Vandenabeele P. Immunogenic cell death and DAMPs in cancer therapy. Nat Rev Cancer. 2012;12(12):860–875.

10. Xi Y, Chen L, Tang J, Yu B, Shen W, Niu X. Amplifying "eat me signal" by immunogenic cell death for potentiating cancer immunotherapy. Immunol Rev. 2024;321(1):94–114.

11. Ruan H, Leibowitz BJ, Zhang L, Yu J. Immunogenic cell death in colon cancer prevention and therapy. Mol Carcinog. 2020;59(7):783–793.

12. Guo W, Zhang C, Zhou Q, Chen T, Xu X, Zhang J, et al. Mitochondrial CCN1 drives ferroptosis via fatty acid β-oxidation. Dev Cell. 2025;60(17):2294–2312.e2211.

13. Jeong SD, Jung BK, Ahn HM, Lee D, Ha J, Noh I, et al. Immunogenic Cell Death Inducing Fluorinated Mitochondria-Disrupting Helical Polypeptide Synergizes with PD-L1 Immune Checkpoint Blockade. Adv Sci (Weinh). 2021;8(7):2001308.

14. Wu W, Luo Y, Sun C, Liu Y, Kuo P, Varga J, et al. Targeting cell-impermeable prodrug activation to tumor microenvironment eradicates multiple drug-resistant neoplasms. Cancer Res. 2006;66(2):970–980.

15. Sugahara KN, Teesalu T, Karmali PP, Kotamraju VR, Agemy L, Girard OM, et al. Tissue-penetrating delivery of compounds and nanoparticles into tumors. Cancer Cell. 2009;16(6):510–520.

16. Murthy RV, Arbman G, Gao J, Roodman GD, Sun XF. Legumain expression in relation to clinicopathologic and biological variables in colorectal cancer. Clin Cancer Res. 2005;11(6):2293–2299.

17. Haugen MH, Boye K, Nesland JM, Pettersen SJ, Egeland EV, Tamhane T, et al. High expression of the cysteine proteinase legumain in colorectal cancer - implications for therapeutic targeting. Eur J Cancer. 2015;51(1):9–17.

18. Liu Z, Xiong M, Gong J, Zhang Y, Bai N, Luo Y, et al. Legumain protease-activated TAT-liposome cargo for targeting tumours and their microenvironment. Nat Commun. 2014;5:4280.

19. Zhou J, Du X, Yamagata N, Xu B. Enzyme-Instructed Self-Assembly of Small D-Peptides as a Multiple-Step Process for Selectively Killing Cancer Cells. J Am Chem Soc. 2016;138(11):3813–3823.

20. Cabral H, Matsumoto Y, Mizuno K, Chen Q, Murakami M, Kimura M, et al. Accumulation of sub-100 nm polymeric micelles in poorly permeable tumours depends on size. Nat Nanotechnol. 2011;6(12):815–823.

21. Ellerby HM, Arap W, Ellerby LM, Kain R, Andrusiak R, Rio GD, et al. Anti-cancer activity of targeted pro-apoptotic peptides. Nat Med. 1999;5(9):1032–1038.

22. Pierschbacher MD, Ruoslahti E. Cell attachment activity of fibronectin can be duplicated by small synthetic fragments of the molecule. Nature. 1984;309(5963):30–33.

23. Dixon SJ, Lemberg KM, Lamprecht MR, Skouta R, Zaitsev EM, Gleason CE, et al. Ferroptosis: an iron-dependent form of nonapoptotic cell death. Cell. 2012;149(5):1060–1072.

692 24. Yang WS, SriRamaratnam R, Welsch ME, Shimada K, Skouta R, Viswanathan
693 VS, et al. Regulation of ferroptotic cancer cell death by GPX4. Cell. 2014;156(1–
694 2):317–331.
695 25. Doll S, Proneth B, Tyurina YY, Panzilius E, Kobayashi S, Ingold I, et al. ACSL4
696 dictates ferroptosis sensitivity by shaping cellular lipid composition. Nat Chem
697 Biol. 2017;13(1):91–98.
698 26. Mancias JD, Wang X, Gygi SP, Harper JW, Kimmelman AC. Quantitative
699 proteomics identifies NCOA4 as the cargo receptor mediating ferritinophagy.
700 Nature. 2014;509(7498):105–109.
701 27. Wang W, Green M, Choi JE, Gijon M, Kennedy PD, Johnson JK, et al. CD8(+) T
702 cells regulate tumour ferroptosis during cancer immunotherapy. Nature.
703 2019;569(7755):270–274.
704 28. Kagan VE, Mao G, Qu F, Angeli JPF, Doll S, Croix CS, et al. Oxidized
705 arachidonic and adrenic PEs navigate cells to ferroptosis. Nat Chem Biol.
706 2017;13(1):81–90.
707 29. Bersuker K, Hendricks JM, Li Z, Magtanong L, Ford B, Tang PH, et al. The CoQ
708 oxidoreductase FSP1 acts parallel to GPX4 to inhibit ferroptosis. Nature.
709 2019;575(7784):688–692.
710 30. Obeid M, Tesniere A, Ghiringhelli F, Fimia GM, Apetoh L, Perfettini JL, et al.
711 Calreticulin exposure dictates the immunogenicity of cancer cell death. Nat Med.
712 2007;13(1):54–61.
713 31. Galluzzi L, Vitale I, Warren S, Adjemian S, Agostinis P, Martinez AB, et al.
714 Consensus guidelines for the definition, detection and interpretation of
715 immunogenic cell death. J Immunother Cancer. 2020;8(1):e000337.
716 32. Michaud M, Martins I, Sukkurwala AQ, Adjemian S, Ma Y, Pellegatti P, et al.
717 Autophagy-dependent anticancer immune responses induced by
718 chemotherapeutic agents in mice. Science. 2011;334(6062):1573–1577.
719 33. Casares N, Pequignot MO, Tesniere A, Ghiringhelli F, Roux S, Chaput N, et al.
720 Caspase-dependent immunogenicity of doxorubicin-induced tumor cell death. J
721 Exp Med. 2005;202(12):1691–1701.
722 34. Apetoh L, Ghiringhelli F, Tesniere A, Obeid M, Ortiz C, Criollo A, et al. Toll-like
723 receptor 4-dependent contribution of the immune system to anticancer
724 chemotherapy and radiotherapy. Nat Med. 2007;13(9):1050–1059.
725 35. Ghiringhelli F, Apetoh L, Tesniere A, Aymeric L, Ma Y, Ortiz C, et al. Activation of
726 the NLRP3 inflammasome in dendritic cells induces IL-1beta-dependent adaptive
727 immunity against tumors. Nat Med. 2009;15(10):1170–1178.
728 36. Panaretakis T, Kepp O, Brockmeier U, Tesniere A, Bjorklund AC, Chapman DC,
729 et al. Mechanisms of pre-apoptotic calreticulin exposure in immunogenic cell
730 death. EMBO J. 2009;28(5):578–590.

Supplementary Files

This is a list of supplementary files associated with this preprint. Click to download.

- SF.docx
- wb.zip